Impact of shrub branches on the shortwave vertical irradiance profile in snow

Florent Domine[1,2,3*], Mireille Quémener[4,5,6*], Ludovick Bégin[4,5,6], Benjamin Bouchard[2,7,8], Valérie Dionne[3,4], Sébastien Jerczynski[4,5,6], Raphaël Larouche[1,5], Félix Lévesque-Desrosiers[1,2,5], Simon-Olivier Philibert[3,4], Marc-André Vigneault[4,5,6], Ghislain Picard[9], Daniel C. Côté[4,5,6]

[1] Takuvik Joint International Laboratory, Université Laval (Canada) and CNRS-INSU (France), Québec City, Canada.
[2] Centre d'Études Nordiques, Université Laval, Québec City, Canada.
[3] Department of Chemistry, Université Laval, Québec City, Canada.
[4] CERVO Brain Research Center, Québec (QC), Canada
[5] Département de physique, de génie physique et d'optique, Université Laval, Québec (QC), Canada
[6] Center for Optics, Photonics and Lasers, Québec (Qc), Canada
[7] Department of Civil and Water Engineering, Université Laval, Quebec City, Canada
[8] CentrEau – Water Research Center, Université Laval, Quebec City, Canada
[9] Université Grenoble Alpes, CNRS, IRD, Grenoble INP, IGE, Grenoble, France

Correspondence to: Florent Domine(florent.domine@gmail.com)
                            Mireille Quémener (mireille.quemener@cervo.ulaval.ca)

Abstract. In the Arctic, shrubs are expanding and are covered by snow most of the year. Shrub branches buried in snow absorb solar radiation and therefore reduce irradiance. This reduces photochemical reaction rates and the emission of reactive and climatically active molecules to the atmosphere. No study is currently available to quantify the reduction in photochemical rates caused by shrubs buried in snow. Here we monitored irradiance at selected wavelengths using filters at 390±125 nm and >715 nm in snow-covered *Alnus incana* (gray alders) shrubs in the boreal forest near Laval University and on nearby grassland during a whole winter by placing light sensors at fixed heights in shrubs and on grassland. Irradiance in shrubs was greatly reduced at 390 nm and much less at 760 nm, where ice is much more absorbent. We performed radiative transfer simulations, testing the hypothesis that shrub branches behave as homogeneous absorbers such as soot. At 390 nm, dense shrub branches are found to reduce irradiance similarly to about 140 ppb of soot. For the >715 nm wavelengths, insufficient data and the greater ice absorption do not allow accurate conclusions. Noting that photochemically active radiation is mostly in the near UV and blue, we calculate that a high branch density will reduce photochemical reaction rates integrated over the whole snowpack by about a factor of two. This may affect the composition of the lower Arctic atmosphere in winter and spring in numerous ways, including a lower oxidative capacity, lower levels of nitrogen oxides and modified secondary aerosol production. Climatic effects are expected from these compositional changes.

1 Introduction

Quantifying the irradiance within the snowpack is of interest for numerous reasons, including metamorphism and photochemistry. Here, we focus on this latter aspect. Chemical reactions in the snowpack lead to the production of numerous species which are released in snowpack interstitial air. Produced species include NO and NO_2 (Honrath et al., 1999), formaldehyde (Sumner and Shepson, 1999), heavier carbonyl compounds and alcohols (Boudries et al., 2002; Houdier et al., 2002) carboxylic acids (Dibb and Arsenault, 2002) and haloalkanes (Swanson et al., 2002). The emission of these species to the atmosphere considerably affects the atmospheric oxidative capacity, ozone and aerosol formation (Domine and Shepson, 2002; Grannas et al., 2007; Finlayson-Pitts and Pitts, 1993), with potential climatic effects because ozone is an important greenhouse gas (Worden et al., 2008) and aerosols scatter light and act as could condensation nuclei (Farmer et al., 2015). Quantifying snowpack emissions to the atmosphere caused by photochemistry requires the knowledge of the irradiance profile in the snowpack (France et al., 2010).

Most snowpack photochemical reactions are triggered by radiation in the 300 to 450 nm wavelength range (Grannas et al., 2007; Wang, 2021), so that spectral data is required to investigate this topic. Vertical profiles of spectral irradiance have been measured in snow containing light-absorbing impurities in the form of deposited aerosols (King and Simpson, 2001; Simpson et al., 2002; France et al., 2011b; France et al., 2011a; Picard et al., 2016). In the Arctic, shrubs are expanding (Sturm et al., 2001a; Ropars and Boudreau, 2012; Ju and Masek, 2016) and the thin Arctic snowpack usually does not extend above the top of shrubs, especially in the high Arctic, where shrubs rarely exceed 50 cm in height (Domine et al., 2016; Sturm et al., 2001b; Marsh et al., 2010) so that buried shrub branches affect light propagation there. The interest of understanding light propagation in snow with shrub branches therefore increases as climate warms, for the climate-relevant reasons mentioned above. Vertical spectral irradiance profiles have been measured by (Belke-Brea et al., 2021) in the low Arctic within shrubs and in snow without shrubs. The shrubs were dwarf birch (*Betula glandulosa*) whose branches are very supple and were bent far below the snow surface so that their effect on irradiance did not extend over the whole snowpack. The impact of shrubs on photochemistry thus cannot be simply evaluated in this case.

To contribute to the understanding of shrub effects on irradiance profiles in snow, and to deduce the resulting impact on photochemical reaction rates in the snowpack and their potential consequences on atmospheric chemistry, we have monitored visible light fluxes at wavelengths centered on 390 nm (blue) and 760 nm (red) in snow with shrubs (*Alnus incana*) and in nearby sites without shrubs during the whole 2020-2021 winter. The 390 nm wavelength is within the most photoactive wavelength range and the ice optical properties do not vary much within this range (Picard et al., 2016) so that findings at 390 nm probably apply reasonably well to the whole photochemical range. At 760 nm, photochemistry is not known to be active for most molecules (Grannas et al., 2007; Wang, 2021). However, at this wavelength, the ice absorption coefficient is about 120 times greater than at 390 nm (Picard et al., 2016), so that investigating this longer wavelength informs us on the impact of shrubs under more absorbing ice conditions.

We deployed custom-made 390 and 760 nm light sensors at fixed heights at regular intervals before snow onset. We thus obtained irradiance data in snow with and without shrubs. Using the data and radiative transfer simulations, we were able to quantify the impact of shrubs on light propagation and on depth-integrated light fluxes in the snowpack.

2 Instruments and Methods

2.1 Optical sensors

Each optical sensor consists of a frosted spherical polystyrene sphere 7 mm in diameter (Cospheric). The sphere had been perforated to its center to insert two plastic optical fibers with 1500 μm core diameter and 15 μm-thick cladding (Toray Industries, PGR-FB1500). The two optical fibers were inserted into a stainless-steel tube of gauge 6G (Component Supply, HTX-06T) to provide rigidity and protect the interface of the fibers and the plastic sphere (Fig. 1). The tube was completely covered with teflon up to the base of the sphere to mimic the snow reflectivity and to prevent water from seeping into the tube and damaging the optical fiber. The assembly, consisting of the sphere, the fibers, and the tube, was then inserted into a PVC mount, and the fibers were routed to a junction box on the ground (Fig. 1).

Inside the junction box, each fiber end was connected to a photodiode (Vishay, TEMD5080X01) which was mounted on a custom-designed printed circuit board (PCB). Blue and red optical filters (Hoya B390 and SCHOTT RG715) were glued with UV light cure adhesive (Loca TP2500) directly to the photodiode sensors. The blue filter has a transmission band centered at 390 nm with a bandwidth of 125 nm. We refer to the radiation transmitted by this filter as 390 nm (or blue) radiation. The red longpass filter transmits light above 715 nm, up to the wavelength allowed by the photodiode, around 1000 nm. We refer to the radiation transmitted by this filter as 760 nm (or red) radiation because 760 nm is near the middle of the relevant range transmitted through snow at significant depths (Warren and Brandt, 2008) and this wavelength was found to be a valid "effective" wavelength for subsequent single-wavelength simulations. The signal received from the photodiodes was conditioned through an amplification and noise-filtering circuit before being transmitted to an Arduino Nano acquisition board. The schematics of the optical assembly is shown in Fig. 1.
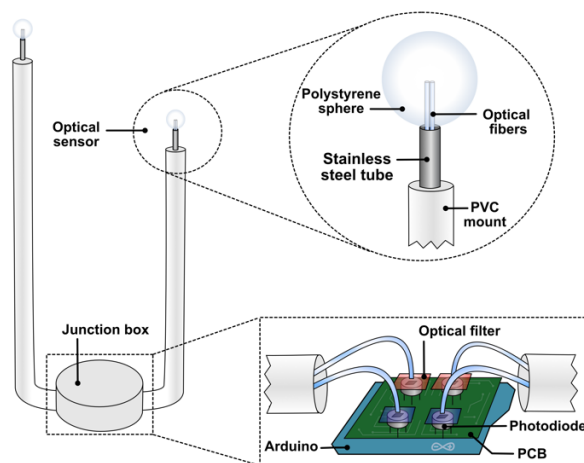
Fig. 1. Schematic of optical sensors. Each assembly consists of two frosted spheres, each housing two optical fibers that are directed to a custom-made printed circuit board (PCB) located in the junction box. Photodiodes collect the signal from the fibers which is filtered by either a blue or red filter.

2.2 Sensor deployment and site description

The sensors, assembled in pairs, were deployed in the Montmorency Forest, the research forest of Université Laval, 60 km north of Québec City. Ideally, an Arctic site would have been preferred. However, the logistical constraints linked to continuous monitoring and data transmission would have been enormous and the risk of instrument failure much greater. In any case, the Arctic was closed to travel at that time because of the COVID 19 pandemic, so that a nearby site was mandatory. The study site (47.3352°N, 71.1375°W, 678 m elevation) featured alder shrubs (*Alnus incana ssp. rugosa*) 1.5 to 2 m high next to a large clearing without erect vegetation, so that shading of the sun was minimal except for very high solar zenith angles (SZA). A set of four sensor pairs located at the tip of PVC mounts of heights 325, 485, 650, 850, 1000, 1200, 1375 and 1550 mm above the ground were placed in the clearing (hereafter F sensors, in the FIELD spot). The heights were selected based on usual peak snow heights at the site, about 2 m, based on the nearby NEIGE monitoring station 1.75 km to the SW at an elevation of 665 m (Pierre et al., 2019). A similar set of eight sensors was placed in four similar shrubs (hereafter S sensors, in the SHRUB spot), about 5 m to the north of the FIELD site (Fig. 2). Several striped poles in view of an automatic time lapse camera were placed in the shrubs and in the field to document snow height evolution. The NEIGE station is equipped with an ultrasonic snow height gauge and a CNR4 radiometer (Kipp & Zonen) which provides broadband (300-2800 nm) downwelling solar irradiance.

It is important to note that each SHRUB sensor had its own peculiar environment within shrub branches. The paired design also imposed constraints on placement. In particular, the 325 mm SHRUB sensor, called S325, was well in the middle of a shrub, with several large branches in its vicinity. The S485 and S650 sensors were closer to the edge of a shrub, with fewer

and smaller branches in their vicinity (Fig. 2). These observations are important for data analysis. Fig. S1 in the Supplement details the positions of the S325 and S485 sensors during installation.
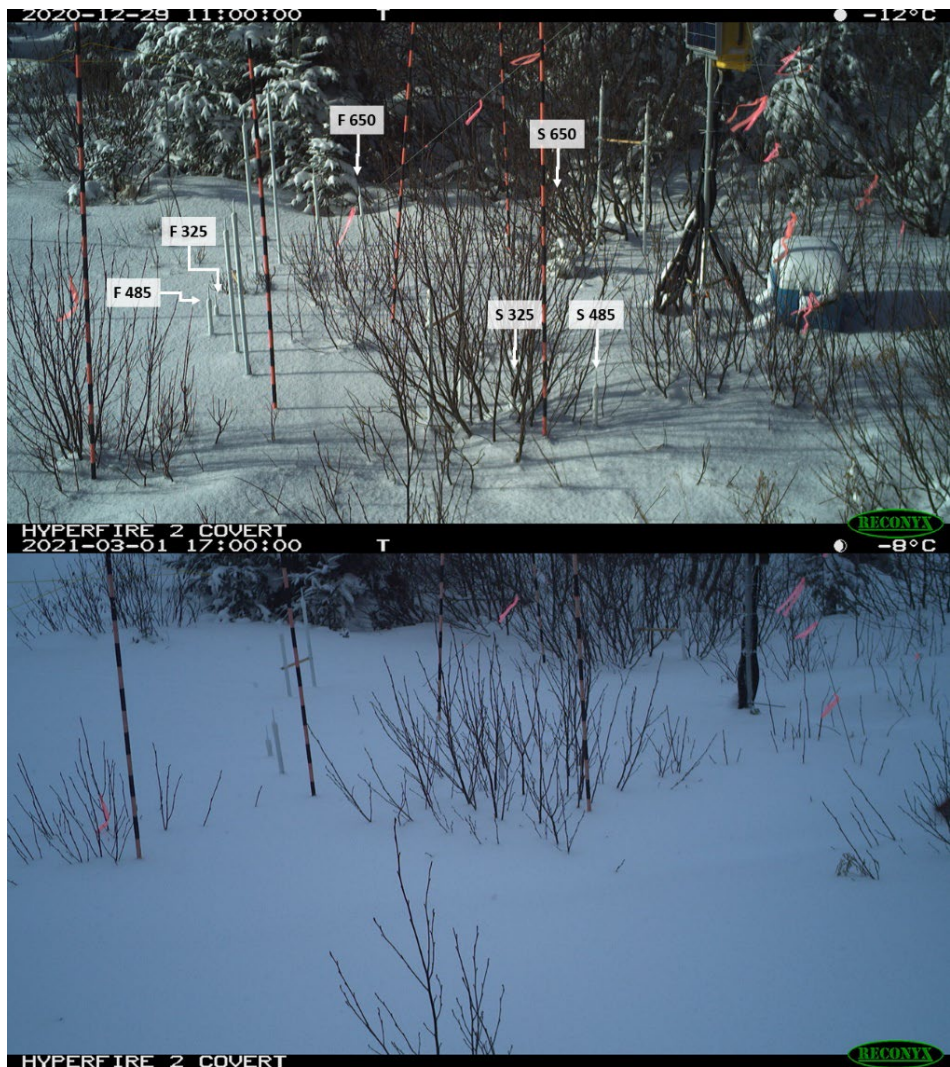
Figure 2. Photographs of the site showing the positions of the sensors. (top) On December 29, 2020, when no sensor was covered by snow. The six sensors whose data were used here are indicated. S325, S485 and S650 are in the SHRUB spot at heights of 325, 485 and 650 mm. F325, F485 and F650 are in the FIELD site. (bottom) Same view at peak snow height on March 1st, 2021, when the six sensors were buried. Note that the snow bent the branches, modifying the branch environment of the S sensors visible on top.

To help quantify branch characteristics, on November 2nd 2022, the morphology of a representative shrub was investigated by measuring the number and diameters of the branches at the heights where our data analysis was focused: 325, 485 and 650 mm. These data can also be used for comparisons with shrubs elsewhere in past and future studies, e.g., (Belke-Brea et al., 2020).

2.3 Electronics, data acquisition and transmission

The schematic of the electronics used for data acquisition and transmission is shown in Fig. 3. As the project involved the deployment of 16 optical sensors, a custom printed circuit board (PCB) was designed to provide a scalable, low-power, and cost-effective solution. Each PCB included four photodiodes (Vishay, TEMD5080X01), four operational amplifier (op-amp) circuits (STMicroelectronics, TSZ124) as well as an Arduino Nano for signal acquisition. The op-amp included a variable gain control on each channel, enabling the adjustment of the output response for each photodiode independently. This adjustment was necessary to ensure that the signal from each photodiode covered the entire 5V input range of the Arduino Nano analog-to-digital converter.

The Arduino Nano in each junction box was equipped with a DHT22 temperature sensor which showed that the temperature at the ground level remained constant near 0°C throughout the winter. No correction for the op-amp temperature-dependant response was thus required. The Arduino Nanos were also connected and powered through USB serial communication with a primary Raspberry Pi (RP1). Each Arduino continuously transmitted raw data from all four photodiodes, along with temperature and humidity readings. This RP1 was equipped with a Python acquisition script programmed to receive the data stream from each Arduino and to compute a single reading per sensor every 10 minutes. This strategy helped limit the size of the files which later needed to be transferred to the server over the internet.

A 3G communication module was added to transfer the data in real-time to a server. However, due to the high-power consumption of the module, a secondary Raspberry Pi (RP2) was used for powering and communicating with this 3G module, while the RP1 managed and powered the eight Arduino Nanos. The RP2 was also tasked to monitor the field with a Raspberry Pi camera (v.1.3) to provide an overall perspective of the study site. These images were transferred to the server in real-time. To minimize the power consumption, a timer relay module (DS1307 real-time clock & SRD-12VDC-SL-C) controlled by an Arduino Nano was used to power both Raspberry Pis. The relay was programmed to keep the Pis powered on during the daytime hours (7AM to 6PM), with a 30-second power interruption every 10 minutes for rebooting and potential bug resolution.
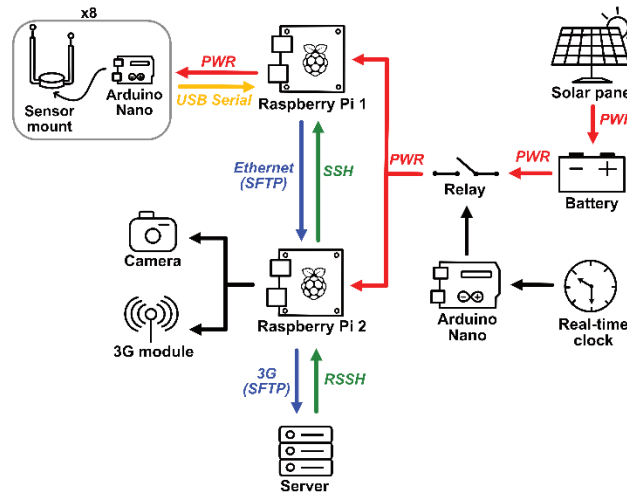
Figure 3. Schematic of the signal acquisition and transmission system. The Raspberry Pi 1 received the data stream from each of the eight sensor pairs, while the Raspberry Pi 2 handled data transmission over internet to the server. The whole system was operated exclusively during daytime hours (7AM-6PM). PWR; Power; SSH: Secure Shell protocol; RSSH: Reverse SSH protocol; SFTP: SSH File Transfer Protocol.

2.4 Snow height determination

An image analysis software which determined the snow level on the striped poles depicted in Fig. 1 was used to determine snow height from photographs taken by a time lapse camera (four photos per day). . To improve the time resolution, the two daily measurements were supplemented with snow height data from the NEIGE station, which provided hourly measurements. Spatial variations between the various striped poles indicate an uncertainty on snow height at the sensors of interest of 1.5 cm.

2.5 Field measurement of snow properties

To constrain inputs into radiative transfer models, vertical profiles of snow properties were measured on January 6th, February 2nd, February 23rd and April 5th 2021. Profiles of density and specific surface area (SSA) were measured at sites near and similar to FIELD and SHRUB. Methods were similar to those described in (Domine et al., 2015). Briefly, a 100 cm^3 density cutter and a field scale were used for density. SSA was determined using the DUFISSS instrument based on the measurement of the infrared reflectance of snow at 1310 nm using an integrating sphere (Gallet et al., 2009).

2.6 Analysis of irradiance data

Our interest is in understanding the irradiance in the snow as a function of depth below the snow surface and of incident solar radiation. The variable of actual interest is the fraction of light incident on the snow surface that reaches the buried sensor. The

signal from each sensor, $I_{r,i}$, was therefore normalized to the incident radiation I_0, which was obtained from sensors that were not buried and whose signal was not saturated. For the blue radiation, we used the average of the $I_{r,i}$ of the three FIELD sensors at heights of 1000, 1200 and 1375 mm to obtain I_{0b}. For the red radiation, the signal from these three FIELD sensors was saturated, so we used the SHRUB sensor at a height of 1550 mm to obtain I_{0r}. There were slight gain variations among sensors. The comparison of signals from all sensors when no sensor was buried and there was just a few cm of snow on the ground in December allowed the homogenization of all the gains. The gain correction factors range from 0.85 to 1.35. For comparisons with simulations, we therefore used gain-corrected data, $(I_{r,i}/I_0)_c$. The detection limit for $I_{r,i}/I_0$ was taken as the signal greater than 3 times the noise, and found to be 0.002.

Under blue sky conditions, most of incident radiation is direct so that the angular response of the sensors used as references must be known. This angular response was measured in the laboratory using a goniometer and was found to be different from a cosine response. Our laboratory measurements allowed correcting for this angular response. However, it was simpler and probably less error-prone to limit our data analysis to overcast conditions, when incident light was diffuse, similar to the conditions of the sensors buried in the snow. Subsequently, we therefore only consider $(I_{r,i}/I_0)_c$ without angular correction, on overcast days. Limiting analysis to overcast conditions is not expected to affect our general conclusions because in snow, light becomes diffuse after a depth of generally a few mm (Simpson et al., 2002). Since our irradiance measurements are all below this depth, the nature of the light incident at the surface (direct vs diffuse) has no impact on our irradiance analysis. Overcast conditions were determined from time lapse images, which revealed the presence of clouds and the lack of shadows, and from the daily time series of solar irradiance, which deviated from the typical clear-sky plots. The normalized irradiance values were obtained by averaging data over several hours when overcast conditions were certain. We estimate the uncertainty on $(I_{r,i}/I_0)_c$ to be 15%, except for values <0.005, when it is about 80%.

The irradiance profiles were simulated using the 'TARTES' Python module (Libois et al., 2013), available at (https://snow.univ-grenoble-alpes.fr/tartes/ last accessed on May 23rd 2024). In TARTES, input data are the thickness, density and SSA of each snow layer, as determined from observations. Additionally, absorption by impurities is considered. What TARTES uses is an absorption coefficient, which can be translated into a concentration of any impurity provided that the mass absorption coefficient of that impurity is known. It may also eventually be translated into a branch density. Here, we translate for simplicity the absorption coefficient used in TARTES into a soot concentration, because soot is a common and highly absorbing impurity in snow (Hansen and Nazarenko, 2004; Chylek et al., 1983; Warren and Clarke, 1990). The soot optical properties used are those reported in (Bond and Bergstrom, 2006), i.e., the soot density is 1800 kg m^{-3} and its complex optical constant is 1.95-0.79i, independent of wavelength. To analyze the effect of shrub branches with TARTES, we consider the soot-equivalent of branches to simulate their absorption. This approach therefore makes the hypothesis that branches behave as a homogeneous absorber such as soot, even though they are discrete absorbers. With this approach, we determine the soot-equivalent of shrub branches by comparing the concentrations of absorbing impurities between the FIELD and SHRUB simulations. At 390 nm, we calculate using TARTES that irradiance is reduced by a factor of 10 at a depth of 29 cm for typical

200   snow encountered during this study (density=200 kg m^{-3}, SSA=25 m^2 kg^{-1}, soot=25 ng g^{-1}). The sensors will therefore be sensitive to optical properties within a radius of ~29 cm.

    Figure 4 sums up the optical properties of the constituents considered here: ice, soot and bark. At 760 nm, ice absorbs 62 times more than at 390 nm (Picard et al., 2016; Warren and Brandt, 2008), as shown in Fig. 4. Soot absorbs 0.51 times as much because of the inverse wavelength dependence of absorption on the imaginary optical index. Regarding bark optical properties,

205   (Juola et al., 2022a) report average reflectance values of several *Alnus incana* individuals and also provide numerical data between 397 and 1000 nm (Juola et al., 2022b). The reflectance is 0.18 at 397 nm and 0.53 at 760 nm (Figure 4). In absorbtivity terms, assuming bark is thick enough, this yields values of 0.82 at 390 nm and 0.47 at 760 nm, a decrease of a factor of 0.57, not very different to the soot value.

    Because of the greater ice absorption, at 760 nm irradiance in snow decreases by a factor of 10 over a distance of 8.2 cm, much

210   shorter than at 390 nm. The corresponding volume is 44 times smaller than at 390 nm. The sensor will therefore be more sensitive to its immediate environment, such as the proximity of a thick branch.

    Even though considering irradiance reduction by a factor of 10 is intuitively simple, the e-folding depth is often considered preferably (France et al., 2011b; France et al., 2010; Simpson et al., 2002). This is the depth over which irradiance is reduced by a factor 1/e=0.368. In the above case, the e-folding depths are 12.5 and 3.7 cm at 390 and 760 nm, respectively. We

215   subsequently consider e-folding depth to quantify light extinction in snow.
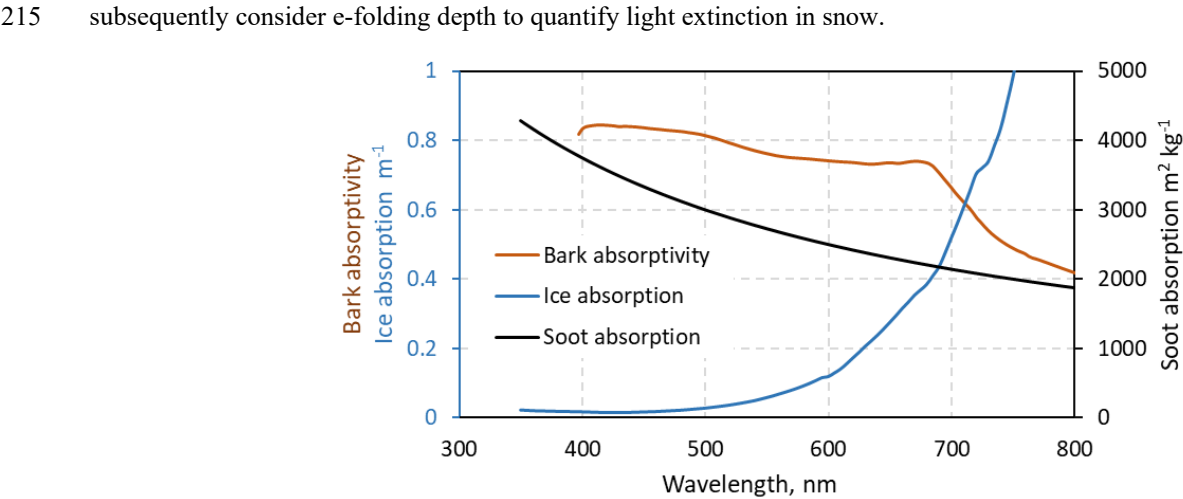
Figure 4. Absorption coefficients of ice and soot used in this study. The absorptivity of *Alnus incana* bark is calculated as 1 – bark reflectivity (Juola et al., 2022b), assuming bark is thick enough to be fully opaque.

3 Results

3.1 Snow properties

Vertical profiles of snow density and SSA measured on February 23rd 2021 at spots similar to FIELD and SHRUB and within 50 m of those spots are shown in Fig. 5. Similar snow data were obtained on January 6th, February 2nd and April 5th. The data obtained on these last two dates are shown in the Supplement, Figs. S2 and S3. The data obtained on January 6th were not used since no sensor was covered at that time and no simulations were performed for that date.
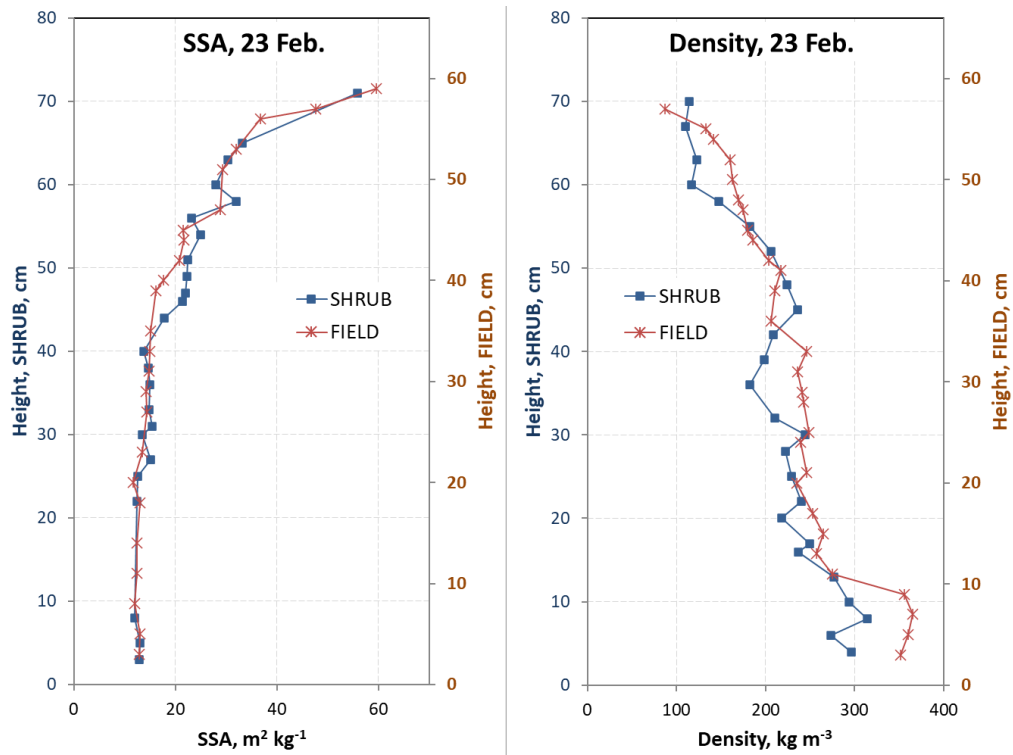
Figure 5. Vertical profiles of snow specific surface area (SSA) and density measured at an open spot similar to FIELD and at a spot in shrubs similar to SHRUB on February 23rd 2021.

The 2020-2021 winter was unusual in that the peak snow height was less than half the usual value (Bouchard et al., 2023) so that most of our sensors were not covered. Time series of snow height, as well as dates selected to perform irradiance simulations, are shown in Fig. 6.
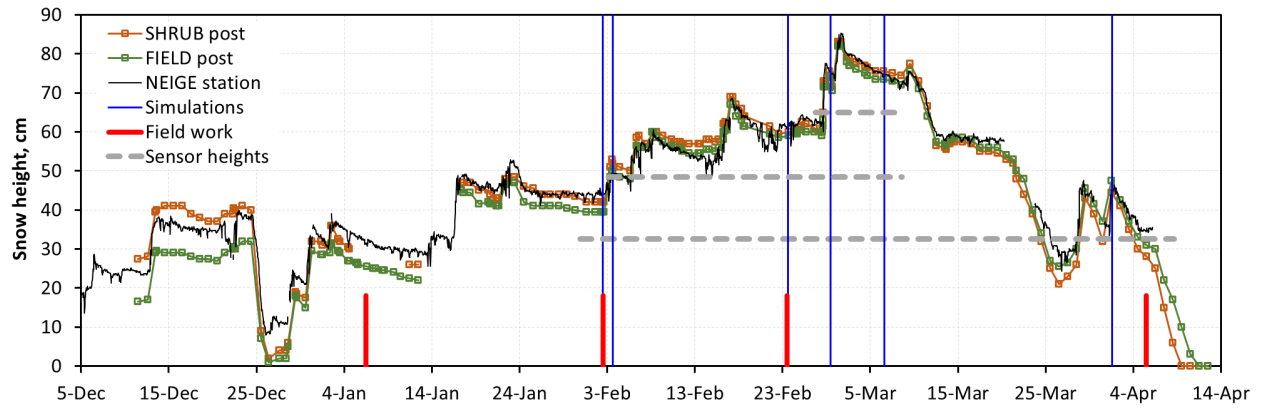
Figure 6. Time series of snow height at the striped poles placed at the study site and determined daily from time lapse images. Snow height monitored by an ultrasonic gauge at the NEIGE station 1.75 km away is also shown. Dates of field work when snow density and specific surface area were measured are indicated with bold red vertical bars. Dates for which irradiance profiles were simulated are noted by thin blue vertical lines. The heights of the three sensors that provided irradiance data have been reported with horizontal dashed lines on the graph.

3.2 Irradiance data

Fig. 7 shows plots of normalized irradiance data $I_{r,i}/I_{0b}$ for i=325, 485 and 650 mm, for both FIELD and SHRUB during the February 28th to March 7th period. This was the only time period when sensors at three heights were buried. The downwelling solar shortwave irradiance measured by the CNR4 radiometer is also shown, which reveals that March 3rd had perfect clear sky whereas March 2nd had clear sky with just a few clouds. The reduced solar radiation on February 28th and time-lapse images show this day was totally overcast. On March 6th, conditions were mostly overcast with rather thin clouds and occasional breaks in the clouds. Periods with direct radiation were removed from the analysis. Both these days were chosen to perform radiative transfer simulations.
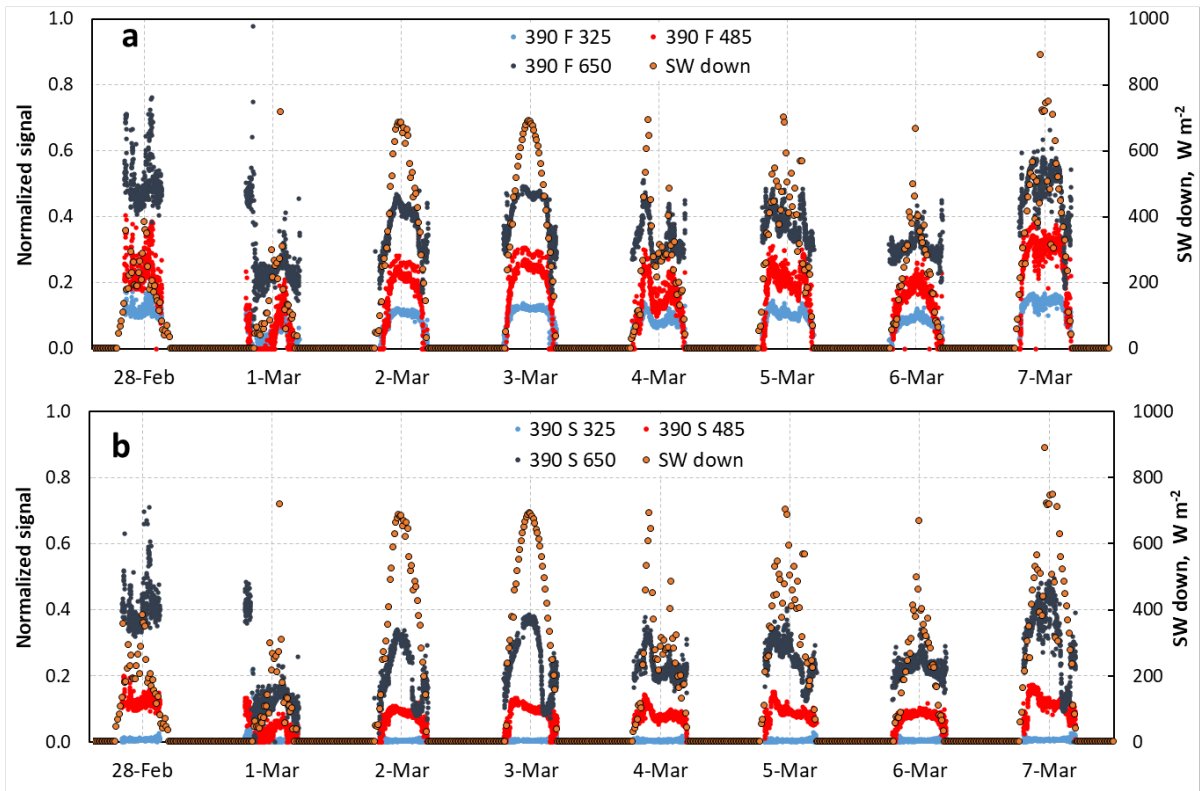
Figure 7. Time series of normalized irradiance $I_{r,i}/I_{0b}$ at 390 nm for the three sensors at 325, 485 and 650 mm heights, when these three sensors were buried. The downwelling solar irradiance (SW down) from the CNR4 radiometer is also shown. (a) FIELD, (b) SHRUB. 390 F 325 is the signal for the 390 nm (blue) wavelength of the FIELD sensor at the 325 mm level. 390 S 325 is the same, but for the SHRUB sensor. SW down is the downwelling shortwave radiation measured by the CNR4.

The signals during both days were determined by selecting periods when conditions were overcast with thick clouds, as shown in Fig. 8. For example, on February 28th at FIELD (Fig. 8a), the signal $I_{r,i}/I_{0b}$ was determined based on data between 10:30 and 12:30. As expected, irradiance signals are lower at SHRUB than at FIELD because of light absorption by shrub branches.

The other days selected for simulations were February 2nd, 3rd and 23rd and April 1st because conditions were overcast. Only one to two sensors were then buried, as visible in Fig. 6. The normalized and gain-corrected experimental irradiance data $(I_{r,i}/I_{0b})_c$ and $(I_{r,i}/I_{0r})_c$ used are reported in the Supplement, Tables S1 and S2.
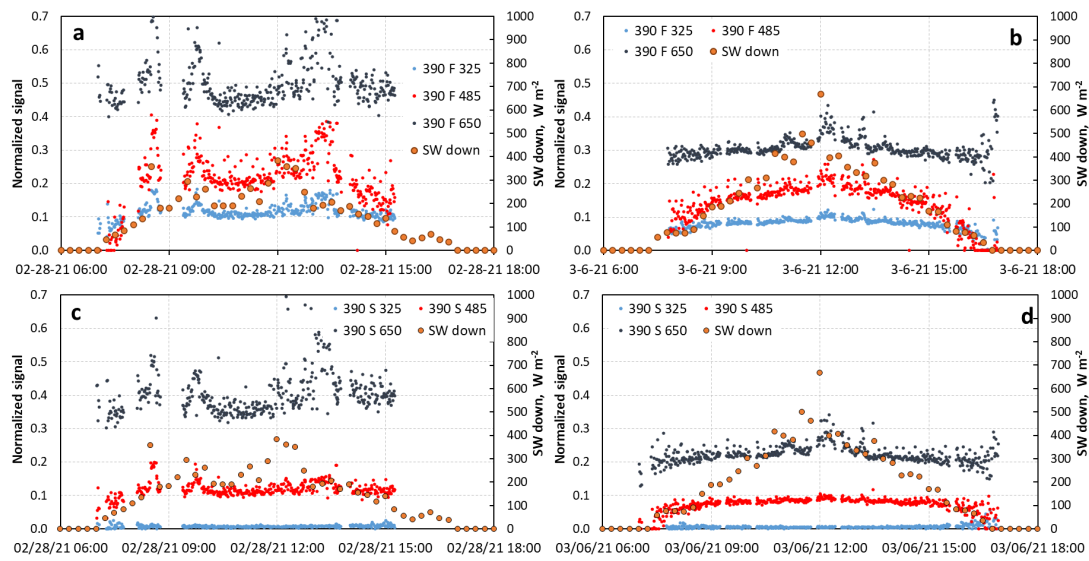
Figure 8. Daily evolution of the normalized irradiance $I_{r,i}/I_{0b}$ under mostly overcast conditions. (a) FIELD, February 28th (b) FIELD, March 6th (c) SHRUB, February 28th (d) SHRUB, March 6th. For the February 28th data, the time range 10:30 to 12:30 was used. For the March 6th data, the time range 7:00 to 16:00 was used, with the exclusion of the 11:30-13:00 time range.

260   Because of the greater ice absorption at 760 nm than at 390 nm (Picard et al., 2016; Warren and Brandt, 2008), radiation penetration is much shallower for red than for blue wavelength and a signal was detected only for the topmost sensor at the red wavelength. $I_{r,i}/I_{0r}$ data at 760 nm obtained from February 28th to March 7th are shown in Fig. 9.
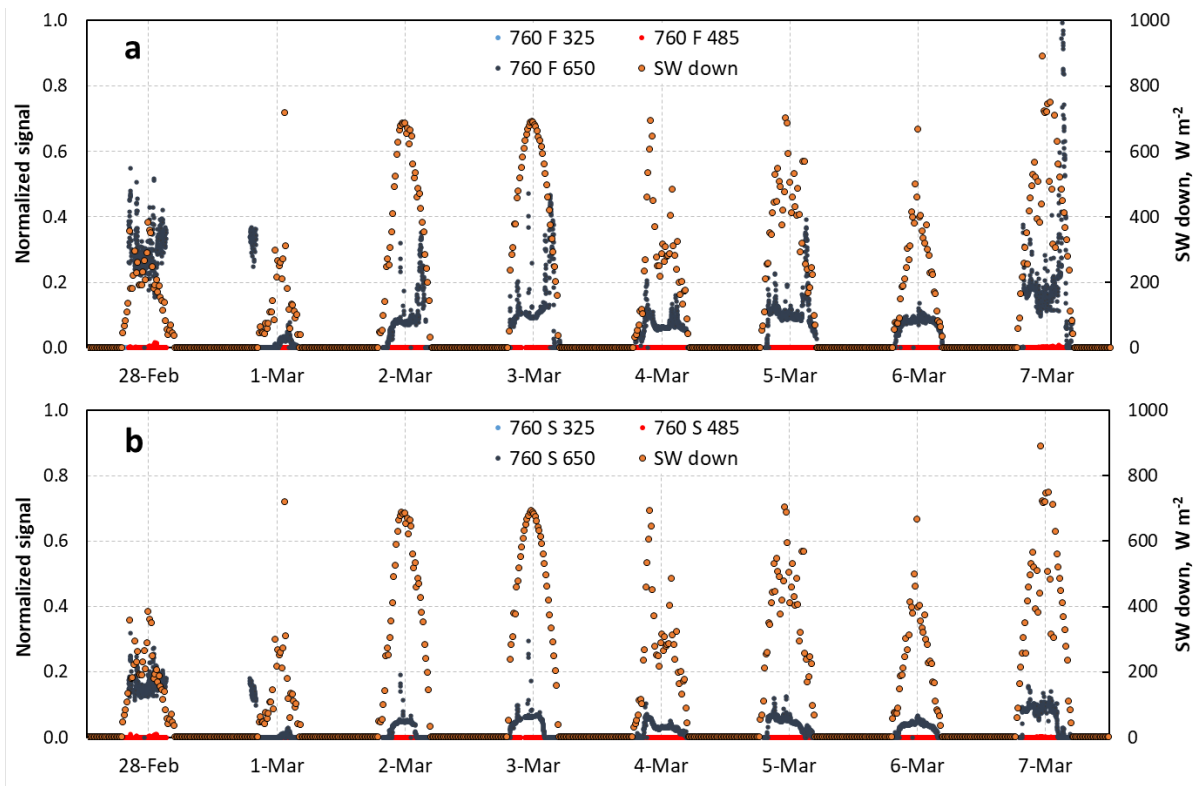
Figure 9. Time series of normalized irradiance $I_{r,i}/I_{0r}$ at 760 nm for the sensors at 325, 485 and 650 mm, when all three were buried. The downwelling solar irradiance (SW down) from the CNR4 radiometer is also shown. (a) FIELD, (b) SHRUB. The signals from the sensors at 325 and 485 mm are too low for detection.

3.3 Shrub morphology

The mean diameter and number of branches of the shrub canopy in a representative shrub at heights of 325, 485, and 650 mm, which correspond to the heights S325, S485 and S650 sensors are reported in Table 1. The distribution of branch diameters at these three heights is shown in Fig. S4. The average canopy diameters at those heights were 75, 110 and 135 cm.

Table 1. Canopy and branch characteristics at heights of 325, 485 and 650 mm heights, corresponding to the level of the three sensors in SHRUB that were buried in snow.

Sensor	Canopy diameter, cm	Number of branches	Mean diameter of branches, mm	Standard deviation of diameter, mm
S325	98	19	14.2	5.3
S485	144	51	7.1	5.4
S650	165	75	5.2	4.2

3.4 Radiative transfer simulations

Irradiance profiles were simulated on February 2nd, 3rd, 23rd and 28th, March 6th and April 1st. An irradiance profile can be simulated if the physical properties (SSA and density) and impurity concentrations of the snow layers are known. For February 2nd and 23rd, we used the snow density and specific surface area values obtained on those very days during our snowpit measurements (Figure 5 and Figure S2). For the other days, snow physical properties were estimated from the snowpit data, the literature (Domine et al., 2007; Taillandier et al., 2007) which helps in estimating the time-evolution of snow physical properties and the SSA-density correlation, and above all from our experience of snow physical properties and their evolution at the Montmorency Forest (Bouchard et al., 2023; Bouchard et al., 2022). The concentration of impurities in the snow, treated as soot-equivalent, was not measured and was used as an adjustable variable to optimize the agreement between measured and simulated irradiance profiles. The main objective of these simulations is to compare the impurity concentrations between FIELD and SHRUB in order to deduce a soot-equivalent for the absorption by shrub branches.

Physical and chemical snow variables used for simulations at 390 nm are reported in Table 2. Layer numbers and boundaries were determined so that density and SSA showed limited variations within a layer (see Figs. 4, S2 and S3). Soot concentrations were determined for each layer on each simulation day. However, the soot concentration of a given layer is not expected to vary significantly over time because soot is not significantly affected by snow metamorphism and by snow chemistry, and soot particles are hydrophobic and little affected by melting events (Festi et al., 2021; Meyer and Wania, 2011). Adjusted soot concentrations were therefore only slightly modified to limit variations in a given layer over time. Variations can indeed occur because of experimental error and can also occur naturally. For example, recrystallization during metamorphism may free an impurity particle embedded into a crystal, so that its location is then on the surface of a crystal, where its absorbing effect is reduced (Kokhanovsky, 2013). Freed particles may also drop to a lower level. The snow physical properties at the sensors' location are also probably slightly different to those at the measurement spots. The values of Table 2 allow a reasonable agreement between simulations and data at 390 nm, as shown in Fig. 10, except on April 1st. Using lower soot values on that last date would allow a perfect fit, but decreasing soot values during melt would not make physical sense. We reflect on this situation in the discussion.

Table 2. Snow density, specific surface area and soot profile values used in radiative transfer simulations using the TARTES model at 390 nm. Snow layers are listed from the top down. Soot values are in part per billion by mass (ppb, ng g^{-1}).

FIELD				SHRUB			
Layer thickness, m	Layer density, kg m^{-3}	Layer SSA, m^2 kg^{-1}	Soot, ppb	Layer thickness, m	Layer density, kg m^{-3}	Layer SSA, m^2 kg^{-1}	Soot, ppb
February 2nd							
0.02	180	34	25	0.02	150	45	150
0.1	210	22	25	0.1	180	27	150
0.1	200	17	25	0.1	210	22	170
0.18	250	15	30	0.2	240	15	170
February 3rd							
0.1	110	75	15	0.1	110	75	100
0.02	180	33	25	0.02	180	33	100
0.1	210	21	25	0.1	200	21	110
0.1	200	17	25	0.1	200	17	160
0.18	250	15	30	0.19	250	15	170
February 23rd							
0.1	140	55	50	0.1	120	50	60
0.1	180	25	10	0.1	200	25	50
0.3	210	15	20	0.3	200	15	150
0.1	350	13	30	0.11	290	13	170
February 28th							
0.125	100	60	20	0.125	90	60	40
0.1	140	40	40	0.1	120	40	60
0.1	180	25	10	0.1	200	25	30
0.3	210	14	13	0.3	210	14	150
0.1	350	13	28	0.12	300	13	170
March 6th							
0.075	150	55	25	0.075	145	58	60
0.07	150	50	25	0.07	145	52	50
0.09	155	37	17	0.09	150	36	25
0.1	180	25	10	0.1	180	25	25
0.3	215	14	11	0.3	215	14	150
0.1	360	13	30	0.12	310	13	170
April 1st							
0.11	120	37	20	0.11	110	37	100
0.1	400	11	20	0.1	320	11	100
0.25	420	5	30	0.22	360	5	170
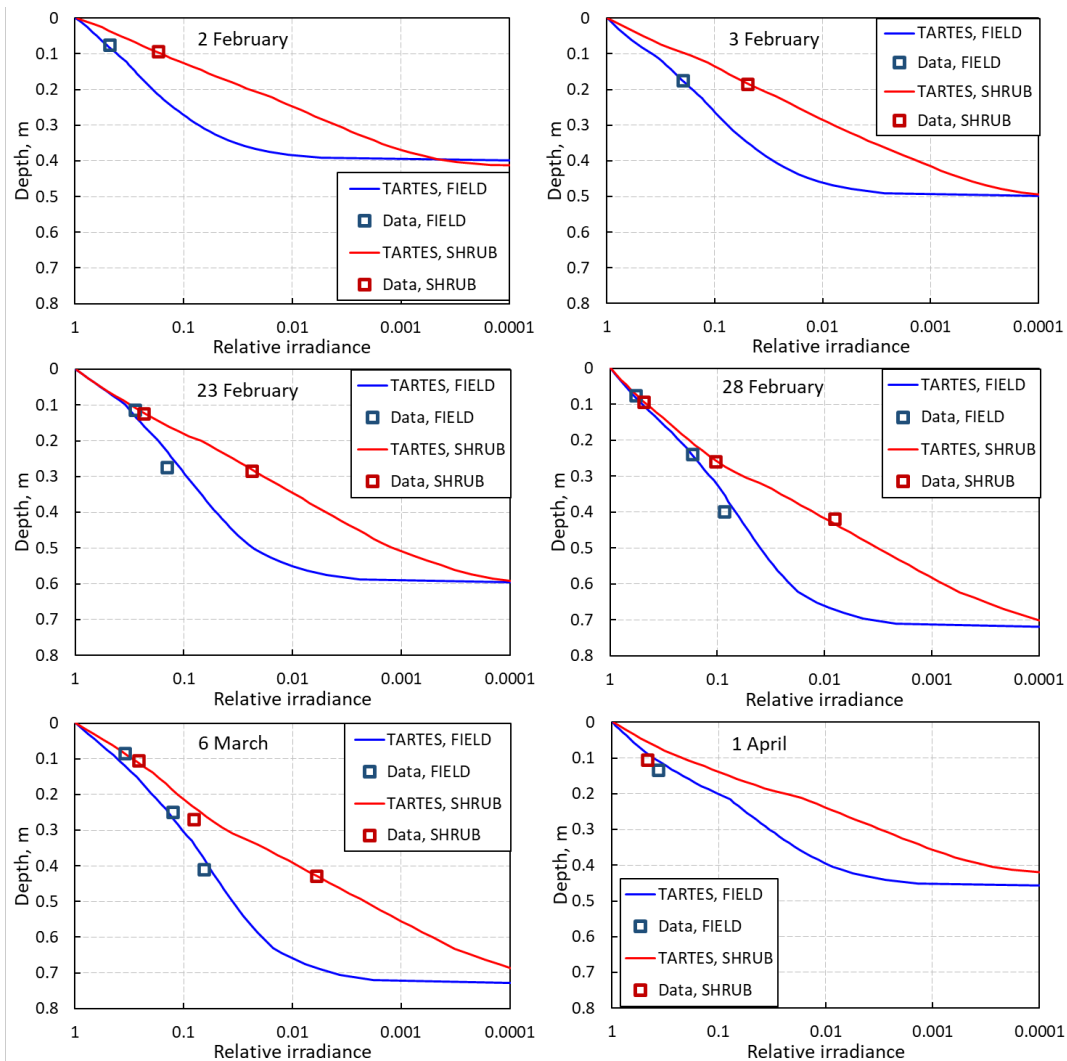
Figure 10. Profiles of irradiance in the snowpack at FIELD and SHRUB at 390 nm simulated by the TARTES software. Experimental data points are also shown. The scale of the Y axis varies because snow depth varied. One to three data points were obtained, depending on the number of sensors buried. The X-scale has been inverted to start at the snow surface. The size of the data points represents the error bars.

For the red radiation, our filter transmits all wavelengths >715 nm. In this range, the absorption coefficient increases with increasing wavelength (Warren and Brandt, 2008): it is 0.52 m^{-1} at 700 nm and 2.1 m^{-1} at 800 nm. Performing simulations over a wavelength range that accounts for dispersion is difficult without knowing the incident spectral irradiance and we rather took the option of choosing an effective wavelength. Simulations with TARTES showed that for wavelengths >850 nm, the signal at 10 cm depth, typical of the position of the topmost sensor, was negligible. The incident irradiance is also depleted in those

wavelengths under cloudy conditions. TARTES simulations using a range of snow physical and chemical properties indicated that 760 nm was a suitable estimate of an effective wavelength for the conditions encountered. TARTES simulations were therefore performed using the 760 nm wavelength optical properties of ice and soot.

For the 760 nm simulations, the same snow physical properties were used as for the 390 nm wavelength. Regarding impurity concentrations, the absorption spectrum of the impurities present here may be different from that of (Bond and Bergstrom, 2006), so that a constant multiplicative factor may have to be used to adjust all soot concentrations at 760 nm. For FIELD data, it was found that this factor was 1, suggesting that most impurities present in the snow were probably soot with optical properties similar to those of (Bond and Bergstrom, 2006). Fig. 4 indicates that bark absorptivity decreases by a factor of 0.57 between 397 and 760 nm, not very different to the factor for soot in this same wavelength range: 0.53. Given the variability in bark properties of individual trees however (Juola et al., 2022a), the bark factor may be different in our specific case.
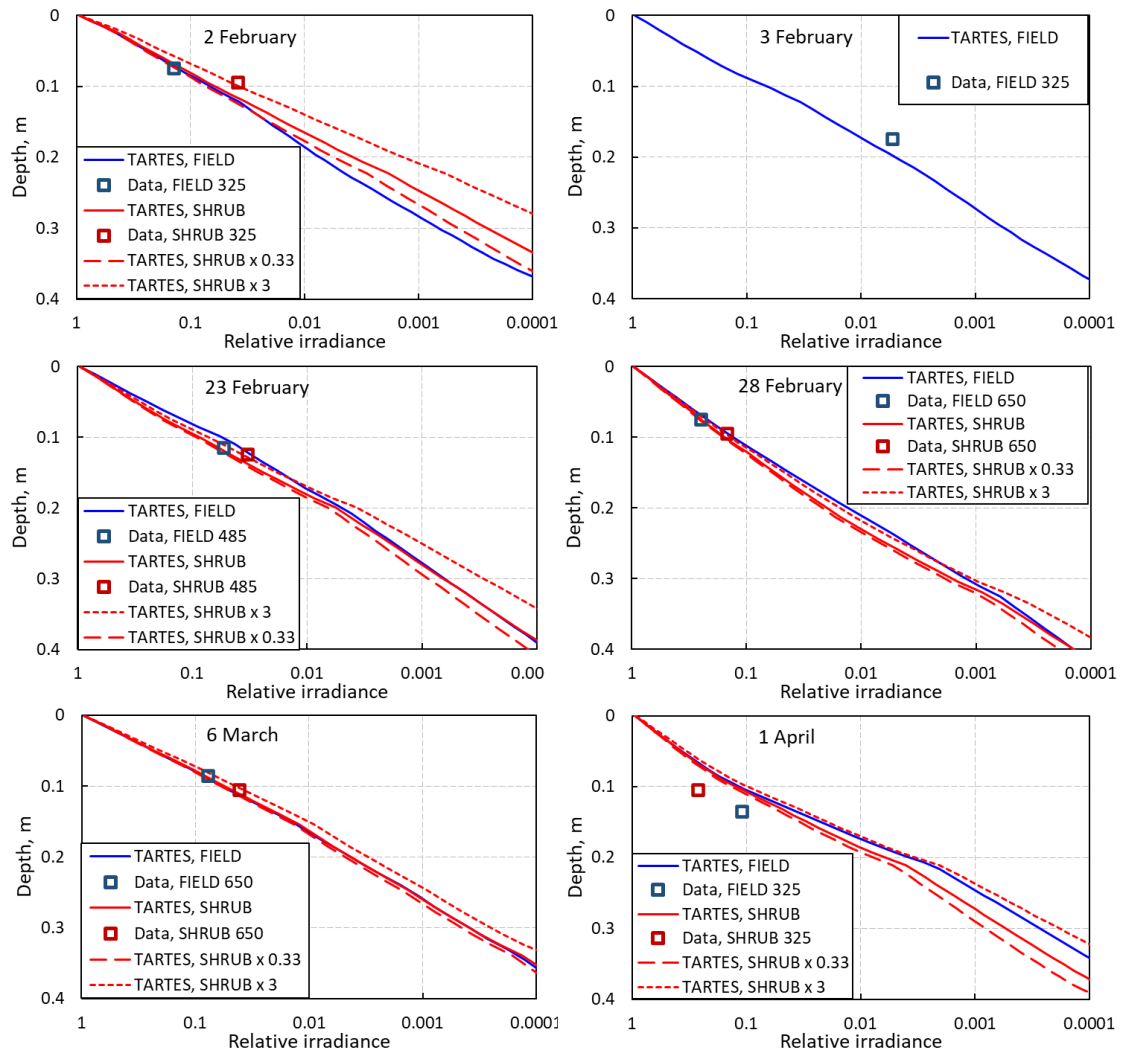
Figure 11. Profiles of irradiance in the snowpack at FIELD and SHRUB at 760 nm. Experimental data points are also shown. Only the topmost sensor produced a detectable signal. Sensors levels in mm are indicated in the legend of each panel. For SHRUB, simulations with impurity concentrations multiplied by 0.33 and 3 are also shown.

We therefore performed simulations at 760 nm using the same soot concentrations for SHRUB as at 390 nm. To investigate the impact of bark optical properties that would vary with wavelength differently to soot, we also performed simulations with concentration multiplied by 0.33 and by 3. Results of simulations at 760 nm are shown in Fig. 11, for sensors for which there was a detectable signal. For the February 3rd data, the 325 mm sensor was 185 mm below the snow surface, and its signal was below detection limit. The corresponding curve is therefore not shown.

4 Discussion

4.1 Snow modification by melting on April 1st

The April 1st data do not show any effect of shrubs branches on irradiance and simulations do not agree with data, while the agreement is good for all other dates. We hypothesize that the intense melting event that occurred between March 9th and 26th and on March 31st (see the rapid snow height decreases in Fig. 6) led to the formation of percolation channels that perturbed radiative transfer differently at FIELD and SHRUB. These channels form ice fingers made up of highly clustered large grains (see e.g. Fig. 6 of (Bouchard et al., 2024)) which scatter light much less than the snow used in the simulations, therefore increasing irradiance at depth. Radiative transfer then cannot be simulated using plane-parallel snow layer geometry as done here. We therefore exclude the April 1st data from subsequent analysis.

4.2 Soot equivalent of shrub branches at 390 nm

The extra extinction at SHRUB relative to FIELD is mostly due to absorption by branches, and to a much lesser extent by different snow physical properties. By subtracting the FIELD soot values to those of SHRUB in Table 2, it appears that the soot equivalent of shrub branches at 390 nm is 125 to 145 ppb for the lower 40 cm of the snowpack. It is 10 to 85 ppb for the upper layers, with most values in the lower part of this range. This is consistent with the positions of the sensors. The 325 mm sensor is in the middle of a shrub and is affected by a greater number of branches than both upper sensors, which are closer to the edge of a shrub as illustrated in Fig. 1 and Fig. S1.

4.3 Soot equivalent of shrub branches at 760 nm

It is noteworthy that the 760 nm simulations for FIELD reproduce the data well using the values used at 390 nm without any adjustment. This supports the validity of our approach and the choice of the 760 nm wavelength as an effective wavelength. At SHRUB, Fig. 11shows that on February 23rd and 28th and on March 6th, branches affect irradiance profiles in a negligible manner and changing the impurity concentrations by a factor of 3 has a negligible impact on irradiance at the sensors' depths. Data from those dates are from the S485 and S650 sensors, which are in low branch density spots. Given the short e-folding depth at 760 nm, the sensors are not affected by branches further away. Since ice is a significant absorber at 760 nm, the main absorber under these conditions is ice and it is therefore not possible to quantify precisely the weak extra extinction caused by branches. On February 2nd on the contrary, the S325 sensor is in a high branch density area and branch impact on the absorption profile is clearly visible. The fit that best reproduces the data is that with a soot concentration multiplied by 3 (Fig. 10). This could be interpreted by a stronger absorption of bark at 760 nm than at 390 nm, contrary to the data of Fig. 4. An alternative explanation is to note that, as shown in Fig. S1, the S325 sensor has several branches within an e-folding depth at 390 nm (12.7

cm), so that here branches have an important contribution to extinction. At 760 nm, the short e-folding depth (3.7 cm) implies that the signal is very sensitive to the immediate environment. It is likely that the extinction must be interpreted in terms of nearby branch density rather than in terms of bark optical properties. In other words, while at 390 nm data appear consistent with our hypothesis that branches can be treated as a homogeneous absorber with well-defined optical properties because the sensor then probes a large volume, this does not seem to be the case at 760 nm where the immediate proximity of branches determines extinction more strongly than bark optical properties.

4.4 Impact of shrubs on irradiance in snow

Figs. 9 and 10 illustrate that irradiance decreases faster with depth at SHRUB than at FIELD. This effect is mostly due to the presence of branches but also, to a lesser extent, to different snow physical properties. To isolate the contribution of branches, we calculate irradiance profiles at SHRUB with the same snow physical properties as at FIELD, but with the SHRUB equivalent-soot concentration. This allows us to determine the extinction caused by branches at 15 cm depth. The extinction factor for the case of high branch density was calculated with the February 2nd data, while the case of low branch density was calculated with the February 28th data. Results are summed up in Table 3. The 760 nm factors were calculated assuming that the spectral dependence of bark absorption was similar to that of soot. Table 3 shows that the radiative impact of a low branch density is very limited, while a high branch density reduces irradiance at 15 cm depth by a factor a 4.33 at 390 nm, a high value.

Table 3. Radiation attenuation factor caused in snow by branches of low (Feb. 28th data) and high (Feb. 2nd data) densities at 15 cm depth. The radiation e-folding depth for the snowpack of February 2nd is also indicated.

	390 nm	760 nm
High branch density	4.33	1.42
Low branch density	1.32	1.05
e-folding depth, cm	11.1	3.4

Based on photographs of the S325 and S485 sensors taken during installation (Fig. S1) and also on the data of Fig. S4 in the Supplement, we attempt to estimate the number and mean diameter of branches within two e-folding depths of each sensor, for both wavelengths studied. These estimates are reported in Table 4. A strict proportionality between branch surface area within the distance of two e-folding depths and the attenuation factors of Table 3 is not expected because a full analysis would require 3-D radiative transfer modeling. However, it is clear that there is a reasonable correlation between Tables 3 and 4. We can even tentatively estimate that 4 branches of 15 mm diameter within a distance of 22 cm from the sensor is roughly

equivalent to 140 ppb of soot for the 390 nm radiation. The 760 nm data show that branches only have a local effect and that only high branch densities will detectably affect 760 nm irradiance in snow.

Table 4. Number of branches and their mean diameter within a radius of two e-folding depths for the S325 and S485 sensors, for both wavelengths studied.

Sensor	390 nm		760 nm	
	No. of branches	Mean diameter	No. of branches	Mean diameter
S325	4	15 mm	1	15 mm
S485	3	8 mm	1	6 mm

4.5 Impact of branches on snowpack photochemistry

In the Arctic, the snow height usually does not extend beyond shrub height, as often observed (Lafleur and Humphreys, 2018; Domine et al., 2016) and illustrated in Fig. S5 in the Supplement, because the trapping of wind-blown snow stops when most branches are buried. Therefore, the incident flux onto the snow surface is similar on snow with and without shrubs. Photochemical reaction rates in any medium depend on irradiance. For species of atmospheric interest, the most active spectral region is the near UV where many molecules have absorption bands (Finlayson-Pitts and Pitts, 2000). The ice absorption coefficient varies little between 350 and 450 nm (Picard et al., 2016) so that the data obtained here at 390 nm may be used to obtain a first estimate of the impact of shrub branches on photochemical reaction rates. By integrating the irradiance over the depth of the snowpacks, the ratios of the rates SHRUB/FIELD have been calculated for the various snowpacks studied here. In this case, we used the different snowpack physical properties for FIELD and SHRUB of Table 2, because this difference is caused by the presence of shrubs (Domine et al., 2016). Results are shown in Table 4.

Table 5. SHRUB/FIELD photolysis ratio in the snowpacks studied at five dates. Similar incident flux values are used for SHRUB and FIELD.

Date	2 Feb.	3 Feb.	23 Feb.	28 Feb.	6 Mar.
Photolysis rate ratio	0.47	0.57	0.75	0.79	0.68

For low branch density, typical of the environment of the top sensors on February 28th, the integrated flux is reduced by just 21%. For high branch density (February 2nd), the flux is reduced by a factor greater than 2. These estimates assume that branches have a radiative effect similar to homogenous impurities such as soot, an assumption that requires confirmation. In the high Arctic (Domine et al., 2022) and even in the low Arctic (Belke-Brea et al., 2020) shrubs are comparatively shorter than in this study and have thinner but more numerous branches. Furthermore, shrubs there often form dense bushes whose branches overlap, increasing branch densities while in this study, shrubs were isolated. It is therefore likely that the effect of

branches on irradiance evidenced here would be at least as important, possibly more so, as in the Arctic. We therefore speculate that photolysis rates in shrub-covered areas in the Arctic may be reduced by at least 25 to 50%, as in Table 4, and possibly even 75%. Furthermore, since branches are thinner and more numerous, the soot-equivalent approach used here, based on a homogeneous medium approximation, may have an improved validity. We thus suggest that irradiance in shrubs in the Arctic may be less spatially-variable than observed here and that a simple large-scale treatment may be valid.

The composition of the atmospheric boundary layer in polar regions is strongly affected by snowpack photochemistry. For example, concentrations of nitrogen oxides are up to 100 times greater than expected by models that neglect snowpack photochemistry (Davis et al., 2001; Honrath et al., 1999), because they are produced by the photolysis of the nitrate ion contained in the snowpack. These high nitrogen oxides concentrations, together with snowpack photolysis of H_2O_2, (France et al., 2007), increase atmospheric concentrations of the OH radical (Mauldin et al., 2004), which is the main atmospheric oxidant. Decreased integrated irradiance fluxes in the snowpack caused by shrub expansion therefore has the potential to generate major perturbations in the photochemistry of Arctic regions, in particular by increasing the lifetime of numerous species such as organic molecules. Furthermore, changes in this chemistry may impact ozone concentrations, which are strongly affected by the concentrations of both nitrogen oxides and organic compounds (Finlayson-Pitts and Pitts, 1993). Ozone is both a potent greenhouse gas and a strong oxidant, so that the impact of shrub growth on atmospheric gaseous composition is manyfold and complex, with processes contributing to ozone decrease and others to its increase. Besides gaseous concentrations, reduced snowpack photochemistry is also expected to affect the formation of secondary organic aerosols from the atmospheric oxidation of organic compounds (Hallquist et al., 2009). This will impact the number of cloud condensation nuclei (Farmer et al., 2015), cloud droplet size and thus cloud albedo (Twomey, 1977). The reduction of snow photochemical rates by shrub expansion may thus lead to numerous chemical and climatic effects that may deserve further quantification using coupled models of snow and atmospheric chemistry (Toyota et al., 2014; Zatko et al., 2016).

5 Conclusion

The comparative measurements of irradiance in snow with and without shrub branches show that when a high branch density is present, shrub branches produce an irradiance attenuating effect equivalent to about 140 ppb of soot at 390 nm, if the soot has optical properties similar to those mentioned by (Bond and Bergstrom, 2006). Such soot concentrations are those of moderately to highly polluted snow (Wang et al., 2013; Dang et al., 2017). This reduces the rate of snowpack photochemistry by about a factor of 2, with the assumption that branches behave as a homogeneous impurity. At 760 nm, the impact of shrub branches is weaker because ice is then the main absorber. Since ice absorption increases regularly and monotonically between 450 and 760 nm (Warren and Brandt, 2008), we expect the impact of branches to decrease likewise over this spectral range.

Supplement

The supplement contains Tables S1 and S2 and Figures S1 to S5.

Code and data availability

The data used in the simulations have been reported in Table 1, Table S1 and Table S2. The TARTES code is available at https://snow.univ-grenoble-alpes.fr/snowtartes/index.

Author contribution

FD and MQ designed research with input from GP. DCC and FD obtained funding. MQ, LB, BB, SJ, RL, FLD and MAV built the experimental apparatus. GP wrote the radiative transfer simulation code. BB and FLD performed the snow field measurements. SOP measured the sensors optical properties. VD performed preliminary data analysis. FD and MQ analyzed the data and wrote the paper with input from GP. LB, BB, RL, FLD, MAV and DCC commented on the paper.

Competing interest

Florent Domine is a member of the editorial board of The Cryosphere.

Acknowledgements

This research was supported by the Sentinel North program of Université Laval, made possible, in part, thanks to funding from the Canada First Research Excellence. Marie-France Gévry managed the Sentinel North support and provided continuous encouragements. Additional funding was provided by the NSERC-CREATE program "Smart, adaptative and autonomous sensing" (#497040) awarded to D. C. Côté. Stéphane Boudreau kindly performed the species identification of the shrubs used in this study.

References

Belke-Brea, M., Domine, F., Picard, G., Barrere, M., and Arnaud, L.: On the influence of erect shrubs on the irradiance profile in snow, Biogeosciences, 18, 5851-5869, 10.5194/bg-18-5851-2021, 2021.

Belke-Brea, M., Domine, F., Boudreau, S., Picard, G., Barrere, M., Arnaud, L., and Paradis, M.: New Allometric Equations for Arctic Shrubs and Their Application for Calculating the Albedo of Surfaces with Snow and Protruding Branches, J. Hydrometeorol., 21, 2581-2594, 10.1175/jhm-d-20-0012.1, 2020.

Bond, T. C. and Bergstrom, R. W.: Light absorption by carbonaceous particles: An investigative review, Aerosol Sci. Technol., 40, 27-67, 10.1080/02786820500421521, 2006.

Bouchard, B., Nadeau, D. F., and Domine, F.: Comparison of snowpack structure in gaps and under the canopy in a humid boreal forest, Hydrol. Processes, 36, e14681, https://doi.org/10.1002/hyp.14681, 2022.

Bouchard, B., Nadeau, D. F., Domine, F., Anctil, F., Jonas, T., and Tremblay, É.: How does a warm and low-snow winter impact the snow cover dynamics in a humid and discontinuous boreal forest? An observational study in eastern Canada, Hydrol. Earth Syst. Sci. Discuss., 2023, 1-33, 10.5194/hess-2023-191, 2023.

Bouchard, B., Nadeau, D. F., Domine, F., Wever, N., Michel, A., Lehning, M., and Isabelle, P. E.: Impact of rain-on-snow events on snowpack structure and runoff under a boreal canopy, EGUsphere, 2024, 1-40, 10.5194/egusphere-2023-3012, 2024.

Boudries, H., Bottenheim, J. W., Guimbaud, C., Grannas, A. M., Shepson, P. B., Houdier, S., Perrier, S., and Domine, F.: Distribution and trends of oxygenated hydrocarbons in the high Arctic derived from measurements in the atmospheric boundary layer and interstitial snow air during the ALERT2000 field campaign, Atmospheric Environment, 36, 2573-2583, https://doi.org/10.1016/S1352-2310(02)00122-X, 2002.

Chylek, P., Ramaswamy, V., and Srivastava, V.: Albedo of soot-contaminated snow, J. Geophys. Res., 88, 837-843, 10.1029/JC088iC15p10837, 1983.

Dang, C., Warren, S. G., Fu, Q., Doherty, S. J., Sturm, M., and Su, J.: Measurements of light-absorbing particles in snow across the Arctic, North America, and China: Effects on surface albedo, J. Geophys. Res., 122, 10149-10168, 10.1002/2017jd027070, 2017.

Davis, D., Nowak, J. B., Chen, G., Buhr, M., Arimoto, R., Hogan, A., Eisele, F., Mauldin, L., Tanner, D., Shetter, R., Lefer, B., and McMurry, P.: Unexpected high levels of NO observed at South Pole, Geophys. Res. Lett., 28, 3625-3628, https://doi.org/10.1029/2000GL012584, 2001.

Dibb, J. E. and Arsenault, M.: Shouldn't snowpacks be sources of monocarboxylic acids?, Atmospheric Environment, 36, 2513-2522, https://doi.org/10.1016/S1352-2310(02)00131-0, 2002.

Domine, F. and Shepson, P. B.: Air-snow interactions and atmospheric chemistry, Science, 297, 1506-1510, 10.1126/science.1074610, 2002.

Domine, F., Barrere, M., and Morin, S.: The growth of shrubs on high Arctic tundra at Bylot Island: impact on snow physical properties and permafrost thermal regime, Biogeosciences, 13, 6471-6486, 10.5194/bg-13-6471-2016, 2016.

Domine, F., Taillandier, A. S., and Simpson, W. R.: A parameterization of the specific surface area of seasonal snow for field use and for models of snowpack evolution, J. Geophys. Res., 112, F02031, 10.1029/2006jf000512, 2007.

Domine, F., Barrere, M., Sarrazin, D., Morin, S., and Arnaud, L.: Automatic monitoring of the effective thermal conductivity of snow in a low-Arctic shrub tundra, The Cryosphere, 9, 1265-1276, 10.5194/tc-9-1265-2015, 2015.

Domine, F., Fourteau, K., Picard, G., Lackner, G., Sarrazin, D., and Poirier, M.: Permafrost cooled in winter by thermal bridging through snow-covered shrub branches, Nat. Geosci., 15, 5540-5560, 10.1038/s41561-022-00979-2, 2022.

Farmer, D. K., Cappa, C. D., and Kreidenweis, S. M.: Atmospheric Processes and Their Controlling Influence on Cloud Condensation Nuclei Activity, Chem. Rev., 115, 4199-4217, 10.1021/cr5006292, 2015.

505 Festi, D., Schwikowski, M., Maggi, V., Oeggl, K., and Jenk, T. M.: Significant mass loss in the accumulation area of the Adamello glacier indicated by the chronology of a 46m ice core, Cryosphere, 15, 4135-4143, 10.5194/tc-15-4135-2021, 2021.

Finlayson-Pitts, B. J. and Pitts, J. N.: Atmospheric chemistry of tropospheric ozone formation - scientific and regulatory implications, Journal of the Air & Waste Management Association, 43, 1091-1100,
510 https://doi.org/10.1080/1073161X.1993.10467187, 1993.

Finlayson-Pitts, B. J. and Pitts, J. N.: CHAPTER 3 - Spectroscopy and Photochemistry: Fundamentals, in: Chemistry of the Upper and Lower Atmosphere, edited by: Finlayson-Pitts, B. J., and Pitts, J. N., Academic Press, San Diego, 43-85, https://doi.org/10.1016/B978-012257060-5/50005-8, 2000.

France, J. L., King, M. D., and Lee-Taylor, J.: Hydroxyl (OH) radical production rates in snowpacks from photolysis of
515 hydrogen peroxide (H2O2) and nitrate (NO3−), Atmospheric Environment, 41, 5502-5509, https://doi.org/10.1016/j.atmosenv.2007.03.056, 2007.

France, J. L., King, M. D., and Lee-Taylor, J.: The importance of considering depth-resolved photochemistry in snow: a radiative-transfer study of NO2 and OH production in Ny-Alesund (Svalbard) snowpacks, J. Glaciol., 56, 655-663, https://doi.org/10.3189/002214310793146250, 2010.

520 France, J. L., King, M. D., Lee-Taylor, J., Beine, H. J., Ianniello, A., Domine, F., and MacArthur, A.: Calculations of in-snow NO2 and OH radical photochemical production and photolysis rates: A field and radiative-transfer study of the optical properties of Arctic (Ny-Ålesund, Svalbard) snow, J. Geophys. Res., 116, F04013, 10.1029/2011jf002019, 2011a.

France, J. L., King, M. D., Frey, M. M., Erbland, J., Picard, G., Preunkert, S., MacArthur, A., and Savarino, J.: Snow optical properties at Dome C (Concordia), Antarctica; implications for snow emissions and snow chemistry of reactive nitrogen,
525 Atmos. Chem. Phys., 11, 9787-9801, 10.5194/acp-11-9787-2011, 2011b.

Gallet, J.-C., Domine, F., Zender, C. S., and Picard, G.: Measurement of the specific surface area of snow using infrared reflectance in an integrating sphere at 1310 and 1550 nm, The Cryosphere, 3, 167-182, https://doi.org/10.5194/tc-3-167-2009, 2009.

Grannas, A. M., Jones, A. E., Dibb, J., Ammann, M., Anastasio, C., Beine, H. J., Bergin, M., Bottenheim, J., Boxe, C. S.,
530 Carver, G., Chen, G., Crawford, J. H., Domine, F., Frey, M. M., Guzman, M. I., Heard, D. E., Helmig, D., Hoffmann, M. R., Honrath, R. E., Huey, L. G., Hutterli, M., Jacobi, H. W., Klan, P., Lefer, B., McConnell, J., Plane, J., Sander, R., Savarino, J., Shepson, P. B., Simpson, W. R., Sodeau, J. R., von Glasow, R., Weller, R., Wolff, E. W., and Zhu, T.: An overview of snow photochemistry: evidence, mechanisms and impacts, Atmos. Chem. Phys., 7, 4329-4373, 2007.

Hallquist, M., Wenger, J. C., Baltensperger, U., Rudich, Y., Simpson, D., Claeys, M., Dommen, J., Donahue, N. M., George,
535 C., Goldstein, A. H., Hamilton, J. F., Herrmann, H., Hoffmann, T., Iinuma, Y., Jang, M., Jenkin, M. E., Jimenez, J. L., Kiendler-Scharr, A., Maenhaut, W., McFiggans, G., Mentel, T. F., Monod, A., Prévôt, A. S. H., Seinfeld, J. H., Surratt, J. D., Szmigielski, R., and Wildt, J.: The formation, properties and impact of secondary organic aerosol: current and emerging issues, Atmos. Chem. Phys., 9, 5155-5236, 10.5194/acp-9-5155-2009, 2009.

Hansen, J. and Nazarenko, L.: Soot climate forcing via snow and ice albedos, Proc. Nat. Acad. Sci. U.S.A., 101, 423-428,
540 10.1073/pnas.2237157100, 2004.

Honrath, R. E., Peterson, M. C., Guo, S., Dibb, J. E., Shepson, P. B., and Campbell, B.: Evidence of NOx production within or upon ice particles in the Greenland snowpack, Geophys. Res. Lett., 26, 695-698, https://doi.org/10.1029/1999GL900077, 1999.

Houdier, S., Perrier, S., Domine, F., Cabanes, A., Legagneux, L., Grannas, A. M., Guimbaud, C., Shepson, P. B., Boudries, H., and Bottenheim, J. W.: Acetaldehyde and acetone in the Arctic snowpack during the ALERT2000 campaign. Snowpack composition, incorporation processes and atmospheric impact, Atmospheric Environment, 36, 2609-2618, 10.1016/S1352-2310(02)00109-7, 2002.

Ju, J. C. and Masek, J. G.: The vegetation greenness trend in Canada and US Alaska from 1984-2012 Landsat data, Remote Sens. Environ., 176, 1-16, 10.1016/j.rse.2016.01.001, 2016.

Juola, J., Hovi, A., and Rautiainen, M.: A spectral analysis of stem bark for boreal and temperate tree species, Ecology and Evolution, 12, e8718, https://doi.org/10.1002/ece3.8718, 2022a.

Juola, J., Hovi, A., and Rautiainen, M.: A dataset of stem bark reflectance spectra for boreal and temperate tree species, V2 [dataset], DOI:

10.17632/pwfxgzz5fj.2, 2022b.

King, M. D. and Simpson, W. R.: Extinction of UV radiation in Arctic snow at Alert, Canada (82 degrees N), J. Geophys. Res., 106, 12499-12507, 10.1029/2001JD900006, 2001.

Kokhanovsky, A.: Spectral reflectance of solar light from dirty snow: a simple theoretical model and its validation, Cryosphere, 7, 1325-1331, 10.5194/tc-7-1325-2013, 2013.

Lafleur, P. M. and Humphreys, E. R.: Tundra shrub effects on growing season energy and carbon dioxide exchange, Environ. Res. Lett., 13, 10.1088/1748-9326/aab863, 2018.

Libois, Q., Picard, G., France, J. L., Arnaud, L., Dumont, M., Carmagnola, C. M., and King, M. D.: Influence of grain shape on light penetration in snow, Cryosphere, 7, 1803-1818, 10.5194/tc-7-1803-2013, 2013.

Marsh, P., Bartlett, P., MacKay, M., Pohl, S., and Lantz, T.: Snowmelt energetics at a shrub tundra site in the western Canadian Arctic, Hydrol. Processes, 24, 3603-3620, 10.1002/hyp.7786, 2010.

Mauldin, R. L., Kosciuch, E., Henry, B., Eisele, F. L., Shetter, R., Lefer, B., Chen, G., Davis, D., Huey, G., and Tanner, D.: Measurements of OH, HO2+RO2, H2SO4, and MSA at the south pole during ISCAT 2000, Atmospheric Environment, 38, 5423-5437, 10.1016/j.atmosenv.2004.06.031, 2004.

Meyer, T. and Wania, F.: Modeling the elution of organic chemicals from a melting homogeneous snow pack, Water Research, 45, 3627-3637, https://doi.org/10.1016/j.watres.2011.04.011, 2011.

Picard, G., Libois, Q., and Arnaud, L.: Refinement of the ice absorption spectrum in the visible using radiance profile measurements in Antarctic snow, The Cryosphere, 10, 2655-2672, 10.5194/tc-10-2655-2016, 2016.

Pierre, A., Jutras, S., Smith, C., Kochendorfer, J., Fortin, V., and Anctil, F.: Evaluation of Catch Efficiency Transfer Functions for Unshielded and Single-Alter-Shielded Solid Precipitation Measurements, Journal of Atmospheric and Oceanic Technology, 36, 865-881, 10.1175/jtech-d-18-0112.1, 2019.

Ropars, P. and Boudreau, S.: Shrub expansion at the forest-tundra ecotone: spatial heterogeneity linked to local topography, Environ. Res. Lett., 7, 015501, 10.1088/1748-9326/7/1/015501, 2012.

Simpson, W. R., King, M. D., Beine, H. J., Honrath, R. E., and Zhou, X. L.: Radiation-transfer modeling of snow-pack photochemical processes during ALERT 2000, Atmospheric Environment, 36, 2663-2670, 10.1016/s1352-2310(02)00124-3, 2002.

Sturm, M., Racine, C., and Tape, K.: Climate change - Increasing shrub abundance in the Arctic, Nature, 411, 546-547, https://doi.org/10.1038/35079180, 2001a.

Sturm, M., McFadden, J. P., Liston, G. E., Chapin, F. S., Racine, C. H., and Holmgren, J.: Snow-shrub interactions in Arctic tundra: A hypothesis with climatic implications, J. Clim., 14, 336-344, 10.1175/1520-0442(2001)014<0336:ssiiat>2.0.co;2, 2001b.

585   Sumner, A. L. and Shepson, P. B.: Snowpack production of formaldehyde and its effect on the Arctic troposphere, Nature, 398, 230-233, 10.1038/18423, 1999.

Swanson, A. L., Blake, N. J., Dibb, J. E., Albert, M. R., Blake, D. R., and Rowland, F. S.: Photochemically induced production of CH3Br, CH3I, C2H5I, ethene, and propene within surface snow at Summit, Greenland, Atmospheric Environment, 36, 2671-2682, 10.1016/s1352-2310(02)00127-9, 2002.

590   Taillandier, A. S., Domine, F., Simpson, W. R., Sturm, M., and Douglas, T. A.: Rate of decrease of the specific surface area of dry snow: Isothermal and temperature gradient conditions, J. Geophys. Res., 112, F03003, 10.1029/2006jf000514, 2007.

Toyota, K., McConnell, J. C., Staebler, R. M., and Dastoor, A. P.: Air-snowpack exchange of bromine, ozone and mercury in the springtime Arctic simulated by the 1-D model PHANTAS - Part 1: In-snow bromine activation and its impact on ozone, Atmos. Chem. Phys., 14, 4101-4133, 10.5194/acp-14-4101-2014, 2014.

595   Twomey, S.: Influence of pollution on shortwave albedo of clouds, J. Atmos. Sci., 34, 1149-1152, 10.1175/1520-0469(1977)034<1149:Tiopot>2.0.Co;2, 1977.

Wang, S.: Chemistry in snow and ice: what have we learned and what can we do, in: Chemistry in the Cryosphere, edited by: Shepson, P. B., and Domine, F., World Scientific, Singapore, 291-364, 10.1142/12095, 2021.

Wang, X., Doherty, S. J., and Huang, J. P.: Black carbon and other light-absorbing impurities in snow across Northern
600   China, J. Geophys. Res., 118, 1471-1492, 10.1029/2012jd018291, 2013.

Warren, S. G. and Brandt, R. E.: Optical constants of ice from the ultraviolet to the microwave: A revised compilation, J. Geophys. Res., 113, D14220, 10.1029/2007jd009744, 2008.

Warren, S. G. and Clarke, A. D.: Soot in the atmosphere and snow surface of Antarctica, J. Geophys. Res., 95, 1811-1816, 1990.

605   Worden, H. M., Bowman, K. W., Worden, J. R., Eldering, A., and Beer, R.: Satellite measurements of the clear-sky greenhouse effect from tropospheric ozone, Nat. Geosci., 1, 305-308, 10.1038/ngeo182, 2008.

Zatko, M., Erbland, J., Savarino, J., Geng, L., Easley, L., Schauer, A., Bates, T., Quinn, P. K., Light, B., Morison, D., Osthoff, H. D., Lyman, S., Neff, W., Yuan, B., and Alexander, B.: The magnitude of the snow-sourced reactive nitrogen flux to the boundary layer in the Uintah Basin, Utah, USA, Atmos. Chem. Phys., 16, 13837-13851, 10.5194/acp-16-13837-2016,
610   2016.